The FEBS Journal

FEBS PRESS science publishing by scientists

Impact of the access tunnel engineering on catalysis is strictly ligand-specific

Shubhangi Kaushik[1,†], Sérgio M. Marques[1,2,†], Prashant Khirsariya[2,3], Kamil Paruch[2,3], Lenka Libichova[1], Jan Brezovsky[1,2], Zbynek Prokop[1,2], Radka Chaloupkova[1,2] and Jiri Damborsky[1,2]

1 Loschmidt Laboratories, Department of Experimental Biology and Research Centre for Toxic Compounds in the Environment (RECETOX), Faculty of Science, Masaryk University, Brno, Czech Republic

2 International Clinical Research Center, St. Anne's University Hospital Brno, Czech Republic

3 Department of Chemistry, CZ-OPENSCREEN, Faculty of Science, Masaryk University, Brno, Czech Republic

Keywords

de novo protein design; enzyme catalysis; enzyme tunnels engineering; haloalkane dehalogenases; protein engineering

Correspondence

R. Chaloupkova and J. Damborsky, Loschmidt Laboratories, Department of Experimental Biology and Research Centre for Toxic Compounds in the Environment (RECETOX), Faculty of Science, Masaryk University, Kamenice 5/A13, 625 00 Brno, Czech Republic

Fax: +420 549496302

Tel: +420 549493567

E-mails: radka@chemi.muni.cz and jiri@chemi.muni.cz

[†]These authors contributed equally to this work

(Received 12 November 2017, revised 2 February 2018, accepted 20 February 2018)

doi:10.1111/febs.14418

The traditional way of rationally engineering enzymes to change their biocatalytic properties utilizes the modifications of their active sites. Another emerging approach is the engineering of structural features involved in the exchange of ligands between buried active sites and the surrounding solvent. However, surprisingly little is known about the effects of mutations that alter the access tunnels on the enzymes' catalytic properties, and how these tunnels should be redesigned to allow fast passage of cognate substrates and products. Thus, we have systematically studied the effects of single-point mutations in a tunnel-lining residue of a haloalkane dehalogenase on the binding kinetics and catalytic conversion of both linear and branched haloalkanes. The hotspot residue Y176 was identified using computer simulations and randomized through saturation mutagenesis, and the resulting variants were screened for shifts in binding rates. Strikingly, opposite effects of the substituted residues on the catalytic efficiency toward linear and branched substrates were observed, which was found to be due to substrate-specific requirements in the critical steps of the respective catalytic cycles. We conclude that not only the catalytic sites, but also the access pathways must be tailored specifically for each individual ligand, which is a new paradigm in protein engineering and *de novo* protein design. A rational approach is proposed here to address more effectively the task of designing ligand-specific tunnels using computational tools.

Introduction

Enzymes are specialized proteins that catalyze chemical reactions in their active sites. In many cases, the active sites are buried deep in the protein core and can only be reached by substances in their surrounding environment through one or several access tunnels [1,2]. Thus, these molecular tunnels have the potential to precisely control the entry or exit of substrates, products, ions, and solvents [3]. Moreover, their size, geometry, dynamics, and physicochemical properties can strongly influence the enzymes' activity, stability,

Abbreviations

aMD, accelerated molecular dynamics; CD, circular dichroism; CHA, 1-chlorohexane; DCP, 2,3-dichloropropan-1-ol; FP, fluorescence polarization; HAOL, 1-hexanol; HLD, haloalkane dehalogenase; IPTG, isopropyl β-D-1-thiogalactopyranoside; IR, infrared; LIE, linear interaction energy; MD, molecular dynamics; MTPs, microtiter plates; NMR, nuclear magnetic resonance; PDB, Protein Data Bank; SD, standard deviation; SEM, standard error of the mean; TCP, 1,2,3-trichloropropane; TMR, tetramethylrhodamine (HaloTag ligand from Promega).

substrate specificity, and enantioselectivity [4–6]. The catalytic importance of enzyme tunnels has been demonstrated for varied systems, such as tryptophan synthase [7], lipase [8], cytochrome P450s [9], haloalkane dehalogenase (HLD) [10], and polyamine oxidase [11].

Another class of dynamic structures that play important roles in protein functions is that of molecular gates [12]. Generally, molecular gates are formed by residues (often of bulky aromatic amino acids) that can reversibly adopt 'open' and 'closed' conformations. The gates in enzymes, together with the access tunnels, control substrate selectivity by discriminating between various substrate molecules [12,13]. They can regulate the transport of ligands, protect distinct regions of proteins from solvent access, and synchronize molecular processes occurring in remote regions of proteins [14].

Enzymatic catalysis is a complex process that involves multiple reaction steps. The catalytic cycle of an enzyme containing a buried active site necessarily involves the transport of the substrate and its binding to the active site, chemical reactions involving bond breaking and bond formation, followed by the release of the resulting products to the bulk solvent [15]. The slowest (and hence the rate-limiting) step in the overall catalytic cycle of an enzyme may be any of the transport processes involved in substrate entry [16] or product release [17,18], substrate binding to the enzyme active site [16] or one of the catalytic steps.

Enzymes have been widely used for diverse applications, such as the production of pharmaceuticals, fine chemicals, biofuels, and food additives [19]. In many cases, enzymes are tailored by protein engineering to overcome existing natural limitations and introduce new functionalities [20,21]. Notably, *de novo* protein design can introduce novel catalytic functions into selected protein scaffolds [22,23]. For example, enzymes catalyzing Diels–Alder [24] and Kemp elimination [25] reactions have been successfully designed. Apart from designing active sites in existing protein folds, the introduction of functional *de novo* tunnels in protein structures is also possible, and can dramatically affect enzymatic catalysis [26]. Thus, both engineering of existing access tunnels and the introduction of *de novo* tunnels afford numerous possibilities for obtaining more useful and efficient biocatalysts.

Haloalkane dehalogenases (EC 3.8.1.5) catalyze the cleavage of carbon–halogen bonds in halogenated hydrocarbons by a hydrolytic mechanism leading to the corresponding alcohol, a halide ion, and a proton [27] (Fig. 1). These enzymes possess buried active sites connected to the exterior environment by several access tunnels, and modification of these tunnels has had profound effects [28,29]. Engineering of a single residue located in the mouth of an access tunnel of the HLD LinB has resulted in modulation of its enzymatic activity and specificity [30]. The modification of an access tunnel in the HLD DhaA has led to the identification of variants with enhanced stability at high temperatures and in the presence of organic co-solvents although with a decreased activity [29]. Further alterations in the tunnel's geometry resulted in enzyme variants with balanced activity and stability [31]. Moreover, a focused mutagenesis of the access tunnel in DhaA resulted in the identification of a superior variant, DhaA31, with considerably improved activity toward the anthropogenic toxic substrate 1,2,3-trichloropropane (TCP) [28].

In the study reported herein, the main access tunnel of the HLD DhaA31 was semi-rationally engineered to assess the effects of tunnel's properties on the enzyme's activity and kinetics toward structurally diverse substrates. The substrates were two small molecules – 1-chlorohexane (CHA) and TCP – and two fluorescent molecular probes – a CHA-like probe (HaloTag TMR) [32] and a TCP-like probe (Fig. 2). The residue Y176 in DhaA31 was identified as highly influencing the properties of the enzyme's access tunnel, and hence it was selected for site-saturation mutagenesis to modulate the tunnel's properties. The effects of mutations on the enzyme's kinetics with selected substrates and binding rates with corresponding molecular probes were then analyzed. Some of the generated variants displayed dramatic improvements in binding rates. Moreover, the tunnel-affecting mutations had opposite effects on the enzyme's activity toward linear and branched substrates, implying that it is important to tailor the tunnel geometry in a ligand-specific manner. To our knowledge, this is the first study showing opposite effects on different substrates upon the mutation of a single tunnel residue.

Results

Identification of a key residue for modifying the access tunnel

First, DhaA31 was studied computationally to investigate the flexibility of its structure and the dynamics of its access tunnels, and then to identify the critical residues governing the tunnel opening and closure. Because all the access tunnels present in the crystal structure of DhaA31 (PDB-ID 3RK4) are closed (radii $\ll$ 1.4 Å), we performed both classical and accelerated molecular dynamics simulations (MD and aMD,

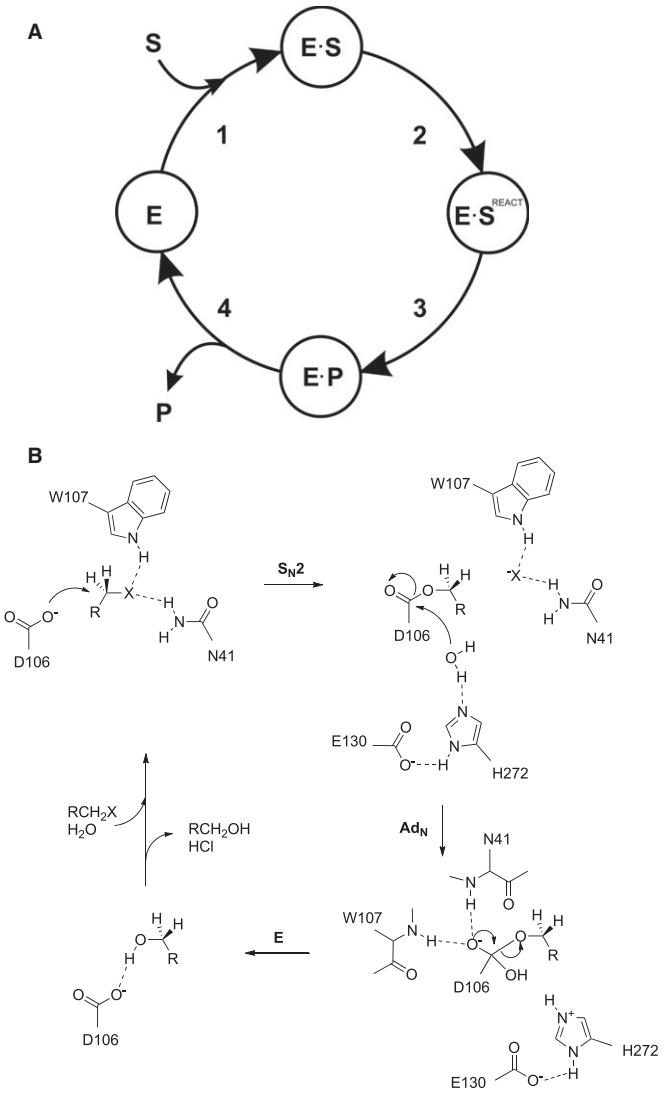

Fig. 1. Catalytic cycle of the HLDs. (A) Schematic representation of the catalytic cycle of the hydrolytic dehalogenation by the HLDs: (1) binding of the substrate S to the enzyme E, resulting in the Michaelis complex, E·S; (2) reorganization of the E·S complex to generate a reactive configuration, $E{\cdot}S^{REACT}$; (3) chemical steps that convert the halogenated substrate into the alcohol and halide products complexed with the enzyme, E·P; (4) release of the products P from the E·P complex. (B) Reaction mechanisms involved in the chemical steps (3) for a halogenated alkane RCH_2X by DhaA; the catalytic steps are: S_N2, bimolecular nucleophilic substitution, Ad_N, nucleophilic addition, and E, elimination. Adapted from Ref. [33,36].

respectively) with DhaA31 (4×500 ns MD and 4×200 ns aMD simulations). All simulations were stable, with RMSD values for the backbone atoms of 0.94 ± 0.08 Å over the four 500 ns MD replicates, and 1.76 ± 0.34 Å for the four 200 ns aMDs. As expected, the structural variation (measured by the fluctuation around the average) was higher for the aMDs than for the MDs due to the higher rates of conformational transitions. This confirms that the aMDs sampled considerably larger conformational spaces than the MDs, and hence they could provide more valuable information regarding infrequent events occurring with this system.

The tunnels were calculated with CAVER 3.02 software [34] for all snapshots in those simulations. Based on the fraction of snapshots with the detected tunnels and the respective opening rates (a tunnel is considered open if its radius is ≥ 1.4 Å), it was found that the only relevant tunnel in DhaA31 is the p1 tunnel, known to be the main tunnel in most HLDs [28,34,35] (Table S1). Some of the parameters obtained for the p1 tunnel in these simulations with DhaA31 are

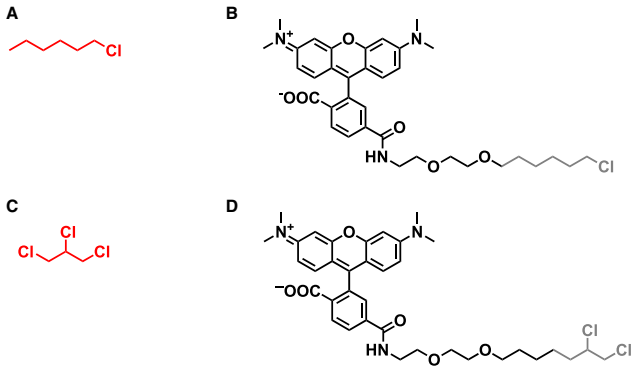

Fig. 2. Molecular structures of (A) 1-chlorohexane (CHA), (B) the CHA-like probe (TMR), (C) 1,2,3-trichloropropane (TCP), and (D) the TCP-like probe.

presented in Table S2. These results show that DhaA31 is flexible enough to allow significant variations of its main tunnel, which can open up to remarkable widths of its bottleneck (~ 3 Å). This may explain the considerable activity of this enzyme toward a wide range of substrates [28]. The p1 tunnel's configuration fluctuated between two extreme conformations in these simulations, corresponding to the closed and open states. The fluctuation was stronger in the aMD simulations than in the MDs (Fig. 3), and the percentage of snapshots in which the tunnel was in the open conformation (where the deviation from the crystal structure with closed tunnel is larger) was higher in the aMDs. The residues defining the tunnel bottleneck were obtained from CAVER (Table S2). Y176 was among the three most frequent residues shaping this bottleneck region during those simulations, suggesting that it plays a critical role in determining the tunnel's dynamics and ability to transport the substances to and from the active site.

An initial *in silico* study aimed at assessing the dynamic properties of several single-point mutants at positions 149, 168, and 176 revealed that the mutants at position 176 displayed the highest variability in terms of tunnel properties (data not shown). We have recently demonstrated the high importance of the residue at the position 176 for the increased activity of DhaA31 toward TCP with respect to the wild-type DhaA (DhaAWT) [36]. Moreover, transient kinetics experiments have revealed that the rate-limiting step in the conversion of TCP to 2,3-dichloropropan-1-ol (DCP) by DhaA31 is the release of the product, which can be impacted by the residue Y176 [36]. All this background considered, the bottleneck residue Y176 was selected for site-saturation mutagenesis to modulate the tunnel properties, aiming at improving the catalytic activity of DhaA31 by changing the rates of ligand exchange. Initially, we expected that the TCP substrate binding and the DCP product release would be coupled for DhaA31, and we thus assumed that enhancing the rate of substrate binding would also improve the rate of product release, and consequently the overall enzymatic turnover.

Construction and screening of the mutant library with saturated position 176

A site-saturation mutagenesis library was constructed by targeting the residue Y176 in an inactive form of DhaA31 [37] using a set of degenerate oligonucleotides to introduce all possible mutations at the selected position. This inactive variant of DhaA31, hereafter referred to as DhaA130, consists of the template DhaA31 with a modified catalytic residue, H272F [32,38]. This mutation will terminate the catalytic reaction at the stage of the alkyl-enzyme intermediate, which allows to easily follow the formation of the enzyme–fluorescent probe covalent complex. The constructed library was cultivated and screened in microtiter plates (MTPs) for altered binding kinetics with the TMR probe using the optimized fluorescence polarization (FP) method, which has successfully captured differences in the binding kinetics of previously studied DhaA variants with modified tunnels [37].

Characterization of mutants using circular dichroism spectroscopy and binding kinetics

The screening of the library resulted in the identification of several mutants with varied binding kinetics. These variants, covering a wide range of binding rates, from fast through moderate to slow, included five single-point mutations (DhaA130 + Y176C, DhaA130 + Y176L, DhaA130 + Y176S, DhaA130 + Y176A,

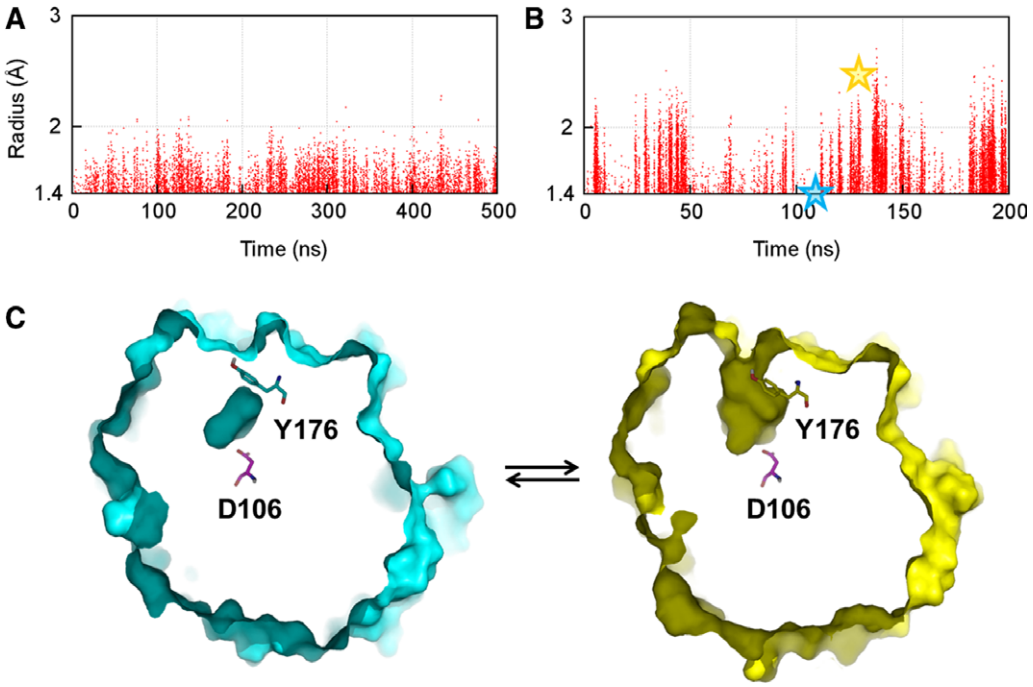

Fig. 3. The main tunnel of DhaA31 and its dynamics. Variation with time of the bottleneck radius in representative MD (A) and aMD (B) simulations. Structures of DhaA31 in closed (cyan) and open (yellow) conformations (C) observed during the aMD simulations (snapshots indicated in B by the stars of corresponding colors), with the bottleneck residue Y176 and nucleophile D106 represented in stick forms.

and DhaA130 + Y176V). These variants were structurally and biochemically characterized and their properties were compared to those of DhaA130. Circular dichroism (CD) spectra recorded in the far-UV region suggested proper folding of the variants (Fig. S1). These variants were then thermally denatured to determine the effects of their respective single-point mutations on thermal stability (Table 1). The Y176L substitution resulted in stabilization of the protein by approximately 4 °C, while the incorporation of Y176S and Y176V substitutions caused destabilization by 2 and 10 °C, respectively. Y176C and Y176A substitutions had no apparent effect on the protein's stability in the test conditions.

The kinetics of the TMR probe's binding to the purified DhaA130 variants was also measured using the FP method to evaluate the effects of each substitution on the enzyme's binding efficiency. The determined binding constants (k_{bind}) of the mutants were compared to that of DhaA130 (Table 2 and Fig. 4). DhaA130 + Y176A showed the highest increase in the binding rate (three orders of magnitude faster than that of DhaA130) of the tested variants, presumably due to the opening of the access tunnel caused by replacing the bulky tyrosine with the smaller alanine residue. The TMR probe's binding rate correlated positively with the predicted opening of the variants' access tunnel ($r_{open.rate}$ = 0.89; Table 2).

Characterization of mutants using steady-state kinetics

To analyze the correlation between the variants' binding rates and the catalytic properties, it was essential to reconstitute their enzymatically active forms. For this purpose, the catalytic residue 272 was converted

Table 1. Melting temperatures of DhaA130 and DhaA31 variants.

Enzyme	T_m (°C)	ΔT_m (°C)
DhaA130	56.0 ± 0.1	–[a]
DhaA130 + Y176C	56.1 ± 0.9	0.1 ± 0.9
DhaA130 + Y176S	54.5 ± 0.7	−1.5 ± 0.7
DhaA130 + Y176V	45.30 ± 0.01	−10.7 ± 0.1
DhaA130 + Y176L	59.6 ± 1.3	3.6 ± 1.3
DhaA130 + Y176A	55.7 ± 0.2	−0.3 ± 0.2
DhaA31	57.6 ± 0.2	–[a]
DhaA31 + Y176C	56.4 ± 0.1	−1.2 ± 0.2
DhaA31 + Y176S	52.8 ± 0.8	−4.8 ± 0.8
DhaA31 + Y176V	49.9 ± 0.0	−7.7 ± 0.2
DhaA31 + Y176L	63.8 ± 0.8	6.2 ± 0.8
DhaA31 + Y176A	54.1 ± 0.7	−3.5 ± 0.7

[a]Not applicable. The SEM values are presented.

Table 2. Tunnel parameters and kinetic properties of selected hits from the site-saturation mutagenesis of DhaA130 and DhaA31 at position 176.

Variant	Static bottleneck radius[a] (Å)	Tunnel opening[b] (%)	Maximum radius[c] (Å)	k_{cat}/K_m[d] TCP ($mM^{-1}·s^{1}$)	k_{cat}/K_m[d] CHA ($mM^{-1}·s^{1}$)	k_{bind}[e] CHA-like probe ($M^{-1}·s^{1}$)
Template	0.97	12.6 ± 1.0	2.32 ± 0.02	1.52 ± 0.28	2.89 ± 0.75	0.39 ± 0.01
Y176L	0.88	1.25 ± 0.25	1.94 ± 0.00	1.83 ± 0.37	2.20 ± 0.64	1.63 ± 0.32
Y176C	1.19	32.3 ± 5.2	2.48 ± 0.05	0.46 ± 0.06	16.9 ± 4.2	28.80 ± 0.45
Y176V	1.33	27.9 ± 2.5	2.50 ± 0.07	0.42 ± 0.08	33.9 ± 1.8	43.50 ± 0.12
Y176S	1.44	64.7 ± 7.4	2.61 ± 0.03	0.15 ± 0.02	22.6 ± 4.7	140.4 ± 3.0
Y176A	1.71	81.0 ± 1.9	2.61 ± 0.00	0.32 ± 0.03	15.5 ± 3.0	405 ± 49
$r_{open.rate}$[f]	0.96	–	0.83	−0.82	0.45	0.89
$r_{max.rad}$[f]	0.85	0.83	–	−0.93	0.70	0.58

[a]Bottleneck radius of p1 tunnel in the static enzyme structures. [b]Rate of tunnel opening (bottleneck radius ≥ 1.4 Å) in the MD simulations. [c]Maximum bottleneck radius during the MDs. [d]Catalytic efficiency of DhaA31 variants toward TCP and CHA. [e]Apparent second order rate of binding of the fluorescent CHA-like probe (TMR) to the corresponding inactive variants containing mutation H272F (DhaA130 variants). [f]Pearson correlation coefficients with the tunnel opening rates ($r_{open.rate}$) or maximum bottleneck radius ($r_{max.rad}$). –, Not applicable. The SEM values are presented when applicable.

from phenylalanine (F272H) back to histidine by site-directed mutagenesis. The resulting active enzymes are referred to as DhaA31 + Y176C, DhaA31 + Y176L, DhaA31 + Y176S, DhaA31 + Y176A, and DhaA31 + Y176V. The CD spectroscopic analysis in the far-UV spectral region confirmed that these variants' folding and secondary structure did not differ significantly from that of DhaA31 (Fig. S1). Thermal denaturation experiments revealed that Y176C, Y176S, Y176A, Y176V substitutions destabilized the DhaA31 protein by 1–8 °C, but the Y176L substitution increased its stability by nearly 6 °C (Table 1).

To study the changes in enzyme activity toward TCP caused by the mutations introduced at position 176, steady-state kinetics of the variants were measured and compared to those of DhaA31 (Tables 2 and 3). The Y176C, Y176A, Y176S, and Y176V substitutions caused an order of magnitude reduction in the turnover number (k_{cat}) compared to that of DhaA31, but their affinity for TCP (as expressed by K_m) was similar or slightly enhanced. These substitutions also considerably suppressed the substrate inhibition. The lower catalytic efficiencies of these variants (expressed by k_{cat}/K_m) relative to DhaA31 were mainly caused by the observed reduction in k_{cat}. In contrast, DhaA31 + Y176L exhibited a slightly improved k_{cat} compared to DhaA31, with no change in K_m, which eventually resulted in the improved catalytic efficiency of this variant toward TCP (Table 3).

Unexpectedly, the Pearson correlation coefficients between the rate of the TMR probe binding to the tested DhaA130 variants and their corresponding active DhaA31 counterparts' catalytic parameters k_{cat} and k_{cat}/K_m were negative (r_{bind} = −0.53 and −0.54, respectively; Table 3). The observed negative correlations may

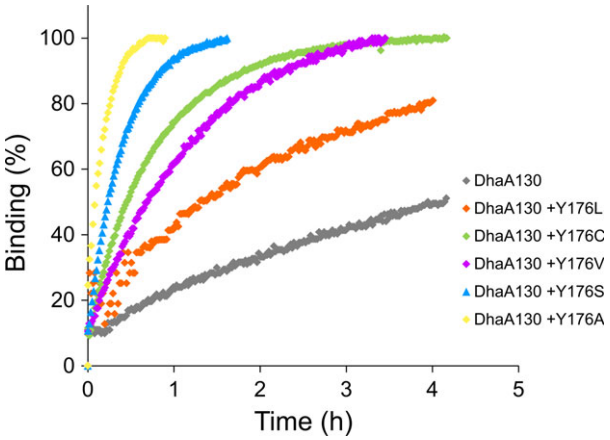

Fig. 4. Binding kinetics of CHA-like probe to the DhaA130 variants.

be due either to the structural dissimilarity between the TMR probe and the TCP substrate or to the fact that the substrate binding and the product release are uncoupled processes for TCP. Thus, the selected enzyme variants were studied with another substrate, CHA, as its alkyl chain mimics the structure of the TMR probe more closely than TCP.

The steady-state kinetics of DhaA31 variants toward CHA was also measured (Tables 2 and 3). A 1.3- to 3.5-fold increase in k_{cat} was observed for all mutants, except DhaA31 + Y176V (which exhibited a similar k_{cat} to DhaA31), and a 2.2–10 fold decrease in K_m was observed for all mutants except DhaA31 + Y176L. The increase in k_{cat} and the accompanying reduction in K_m resulted in improved catalytic efficiencies for DhaA31 + Y176C, DhaA31 + Y176S, DhaA31 + Y176V, DhaA31 + Y176A variants toward CHA, while DhaA31 + Y176L exhibited a similar catalytic

Table 3. Steady-state kinetic parameters of DhaA31 variants toward TCP and CHA.

Substrate	Enzyme	k_{cat} (s^{-1})	K_m or $K_{0.5}$ (mM)	K_{si} (mM)	n	k_{cat}/K_m ($mM^{-1}\cdot s^{-1}$)
1,2,3-trichloropropane (TCP)	DhaA31	1.33 ± 0.11	0.87 ± 0.14	4.89 ± 0.08	–[a]	1.52 ± 0.28
	DhaA31 + Y176C	0.190 ± 0.009	0.412 ± 0.045	42 ± 22	1.5 ± 0.1	0.461 ± 0.055
	DhaA31 + Y176S	0.113 ± 0.005	0.769 ± 0.072	18.2 ± 3.1	1.18 ± 0.02	0.147 ± 0.015
	DhaA31 + Y176V	0.123 ± 0.024	0.294 ± 0.011	140 ± 19	1.44 ± 0.02	0.417 ± 0.083
	DhaA31 + Y176A	0.107 ± 0.007	0.336 ± 0.019	29.2 ± 5.4	1.49 ± 0.02	0.317 ± 0.028
	DhaA31 + Y176L	1.57 ± 0.22	0.86 ± 0.13	2.8 ± 0.2	–[a]	1.83 ± 0.37
r_{bind}[b]		−0.53	−0.45	–[a]	–[a]	−0.54
1-chlorohexane (CHA)	DhaA31	0.057 ± 0.007	0.020 ± 0.005	0.57 ± 0.01	1.37 ± 0.09	2.89 ± 0.75
	DhaA31 + Y176C	0.101 ± 0.015	0.006 ± 0.001	0.26 ± 0.08	1.75 ± 0.24	16.9 ± 4.2
	DhaA31 + Y176S	0.205 ± 0.042	0.0091 ± 0.0004	0.27 ± 0.07	1.42 ± 0.27	22.6 ± 4.7
	DhaA31 + Y176V	0.052 ± 0.002	0.00153 ± 0.00005	0.04 ± 0.02	2.42 ± 0.50	33.9 ± 1.8
	DhaA31 + Y176A	0.143 ± 0.005	0.009 ± 0.002	0.26 ± 0.03	1.41 ± 0.11	15.5 ± 3.0
	DhaA31 + Y176L	0.076 ± 0.007	0.035 ± 0.010	–[a]	1.15 ± 0.10	2.20 ± 0.64
r_{bind}[b]		0.57	−0.32	–[a]	–[a]	0.19

[a]Not applicable. [b]r_{bind}, Pearson correlations of the catalytic parameters for TCP and CHA with the binding constant k_{bind} of the CHA-like (TMR) probe to the respective DhaA130 variants. The SEM values are presented when applicable.

efficiency as DhaA31 (Table 3). We also found positive correlations between the catalytic parameter k_{cat} of DhaA31 variants toward CHA and the binding rates of the CHA-like probe to the corresponding DhaA130 variants (r_{bind} = 0.57; Table 3). The significant differences in these trends compared to those observed for the TCP conversion show that the binding rates and enzyme kinetics are ligand-specific.

The structure–function relationships were analyzed in an attempt to rationalize the steady-state kinetic parameters observed in terms of the physicochemical properties of the introduced amino acid residue (Table S3). It was observed that k_{cat} and k_{cat}/K_m were correlated with the volume, surface area, hydrophobicity, and hydrophilicity of the amino acid residue (absolute coefficient values between 0.5 and 0.9), but not with polarity. Interestingly, the correlations for TCP and CHA substrates with each its property had opposite trends: while k_{cat} and k_{cat}/K_m for the TCP correlated positively with the volume, surface area and hydrophobic character, for CHA it was the opposite. The K_m values for TCP displayed substantially lower correlation coefficients with the same properties than k_{cat}. Interestingly, K_m for TCP and CHA followed the same trends, decreasing with the increase in volume, surface area, and hydrophobic character of the residue 176. This fact demonstrates that the properties of the substituted amino acid have a similar influence on the binding of TCP and CHA. As a consequence, this implies that the step of substrate binding has a different impact on the overall catalytic conversion for these two substrates (as shown by the different effects on the k_{cat} values). The binding rate of the CHA-like probe k_{bind} also showed some correlation with those properties, following the same trend as k_{cat} for the CHA substrate. Overall, according to the above-mentioned correlation coefficients (Table S3), the structure–function relationships suggest that bulkier and more hydrophobic amino acid substitutions at the position 176 accelerate the catalytic conversion of TCP (k_{cat}), but reduce that of CHA, the binding of both substrates (K_m) and the binding of the CHA-like probe (k_{bind}).

Characterization of mutants using pre-steady-state kinetics

Pre-steady-state burst analysis was performed to investigate the rate limitation in the conversion of TCP and CHA by DhaA31. As described earlier by Pavlova *et al.*, the catalytic cycle of DhaA31 toward TCP is limited by the product's release [28], since a clear pre-steady-state burst of both chloride and alcohol products were observed upon rapid mixing of DhaA31 with TCP (Fig. 5A). This suggests that none of the chemical steps leading to the formation of both of the reaction products are rate-limiting for the enzyme. Contrary results were obtained for CHA: the pre-steady-state burst of chloride production and the absence of alcohol product burst observed upon rapid mixing of DhaA31 with CHA indicated that the hydrolysis of the alkyl-enzyme intermediate leading to the formation of the alcohol product is the slow rate-determining step of CHA conversion catalyzed by DhaA31 (Fig. 5B and Table 4). This implies that the access of the water molecules to the active site may have a determining effect on the hydrolysis of CHA by DhaA31.

Analysis of access tunnels using computer simulations

Aiming at a deeper understanding of the structural basis for explaining the mutations' effects on the catalytic hydrolysis of TCP and CHA and on the binding of the fluorescent probe, we have studied the properties of the access tunnels by *in silico* methods. The structures of the target mutants of DhaA31 were constructed using ROSETTA software [39]. MD simulations were then performed with each protein to evaluate the dynamic properties of their structures. CAVER software was used to calculate the tunnels in the initial structures and during the simulations. The results of these calculations are presented in Table 2.

As expected, the main (p1) tunnel in these mutants was highly varied, with bottleneck radii in their static structures ranging between 0.88 and 1.71 Å (Table 2 and Fig. 6). The Y176L and Y176A mutants had the narrowest and the widest tunnels, respectively. The rates of the tunnel opening in the MD simulations were strongly correlated with both the bottleneck radii of the respective static structures ($r_{\text{open.rate}} = 0.96$) and the maximum opening radii observed in each simulation ($r_{\text{max.rad}} = 0.83$). The comparison of the main tunnel's properties with the kinetic parameters yielded interesting correlations (Table 2). The catalytic efficiency ($k_{\text{cat}}/K_{\text{m}}$) of the DhaA31 variants toward TCP was negatively correlated ($r_{\text{open.rate}} = -0.82$) with the tunnel opening rates and the maximum bottleneck radii ($r_{\text{max.rad}} = -0.93$), which means that variants with narrower tunnels are, in general, more active toward this substrate. Conversely, the catalytic efficiency of the enzymes toward CHA was positively correlated with those parameters, especially the maximum radii ($r_{\text{max.rad}} = 0.70$). The binding rates of the CHA-like probe (k_{bind}) to the tested enzymes were positively correlated with the opening rates of the main tunnel ($r_{\text{open.rate}} = 0.89$), reflecting that increases in the rates of tunnel opening promote the binding of the probe, similarly to the trend observed for the catalytic conversion of CHA.

The geometric and dynamic properties of the p1 tunnel are closely related to the volume of the amino acid residue at the position 176 (Pearson correlation factor between volume and the tunnel opening rate of −0.88). For this reason, it was expected that the catalytic and kinetic parameters were also highly correlated with the tunnel radii and tunnel opening rates, but inversely from what had been observed for the volume and hydrophobicity in the structure–function relationships. The relationships discussed here show that the dehalogenation of CHA and the binding of the CHA-like probe are, overall, coupled with the accessibility of the active site to the external environment. However, this is not the case for TCP.

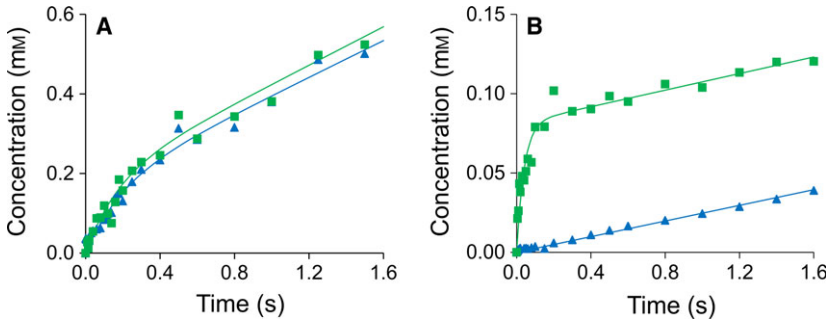

Fig. 5. Rapid quench flow analysis of DhaA31-catalyzed reactions. The burst of the reaction monitored upon mixing 160 μM of DhaA31 with 7500 μM TCP (A) and 690 μM CHA (B). Halide (■) and alcohol (▲) product concentrations were analyzed by ion and gas chromatography, respectively. The solid lines represent the best fits to the kinetic data. [Colour figure can be viewed at wileyonlinelibrary.com]

Table 4. Kinetic parameters of haloalkane dehalogenase DhaA31 with TCP and CHA.

Substrate	k_{burst} (s^{-1})	k_{ss} (s^{-1})	$K_{0.5}$ (mM)	k_{cat} (s^{-1})	n
TCP[a]	5.8 ± 2.3	1.42 ± 0.31	1.2 ± 0.1	1.26 ± 0.07	–
CHA[b]	24.7 ± 3.8	0.158 ± 0.003	0.020 ± 0.005	0.057 ± 0.007	1.37 ± 0.09

[a]Data from previous work [28]. [b]Kinetic parameters were determined at 37 °C and pH 8.6; the rate of halide burst (k_{burst}) and the rate for steady-state phase (k_{ss}) were calculated by fitting the rapid quench data to Eqn (4). –, Not applicable. The SEM values are presented.

In silico analysis of substrate binding and product release

The results of redesigning the molecular tunnel on the enzymatic conversion of TCP and CHA were expected to be connected to the differences in the substrate and product transportation through the same tunnels during the catalytic cycle. However, the changes in the tunnel properties were found to have very different effects on the catalytic hydrolysis of the two substrates by DhaA31 and its variants. This finding demonstrates that TCP and CHA have mechanistically different catalytic bottlenecks. To further investigate these differences, we decided to study the transport of those substrates and the corresponding products through the tunnels of DhaA31 using MD simulations.

We performed MD and aMD simulations of DhaA31 in the presence of TCP and CHA in the bulk solvent at the experimental concentration (three molecules of substrate per protein molecule). The binding of substrate molecules into the protein tunnels was detected in both systems. We observed that any binding or release events with DhaA31 occurred exclusively

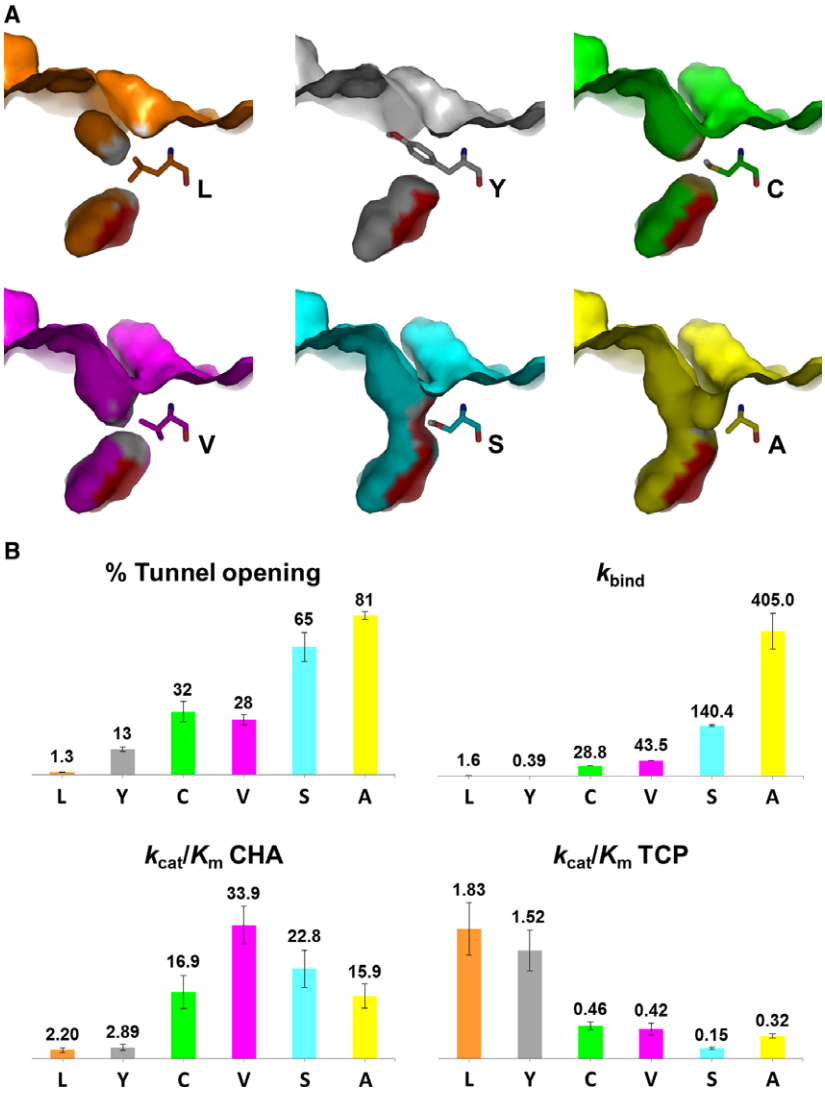

Fig. 6. Illustrative structures and properties of the studied variants. Protein surface showing the p1 access tunnel in the static structures and the respective residues at position 176, ordered by the radii of the tunnel bottlenecks (A). Opening rates (in %) of the p1 tunnel in the MD simulations, binding rate of the TMR probe (k_{bind}, in $M^{-1}\cdot s^{-1}$), and catalytic efficiency (k_{cat}/K_m, in $mM^{-1}\cdot s^{-1}$) of each variant toward CHA and TCP (B). The red parts of the surfaces represent the areas of contact with the catalytic residues. The error bars represent the SEM ($n = 4$ for the tunnel opening rates of DhaA31 and $n = 2$ for the mutants; $n = 3$ for the kinetic parameters).

through the p1 tunnel, confirming its functional importance for the enzyme. This was also reflected in the tunnel's opening rates, which were, in every case, higher than those observed for the unbound DhaA31 (12.6 ± 1.0 in MDs and 17.4 ± 5.4 in aMDs; compare with Table 5), demonstrating that the transit of substances through the tunnel induces its opening [40]. This finding illustrates how enzymes with apparently occluded active sites or very narrow access tunnels can still display catalytic activity due to the substrate and/or product induced-opening of the tunnels. We found that both TCP and CHA could enter DhaA31's main tunnel reaching distances < 6 Å from the active site, even within the timescales surveyed by the MDs (Tables 5 and 6 and Fig. S2). The simulations showed a significantly higher number of binding events with CHA than with TCP (*P* value 0.045 for the aMDs). Consequently, CHA spent significantly more time inside the p1 tunnel (< 9 Å from the active site) than TCP (*P* value 0.002; see Table 5). This is in good agreement with the higher affinity of DhaA31 with CHA as compared to TCP (K_m 0.020 and 0.87 mM, respectively; see Table 3). Moreover, the release of CHA after entering the tunnel (at distances < 6 Å from the active site) occurred in both MD and aMD simulations, but no release of TCP was observed within the time frame of our simulations.

We also performed simulations with DhaA31 containing DCP or 1-hexanol (HAOL) and the chloride products in its active site. No release of DCP from DhaA31 was observed in the MD simulations, while HAOL was released several times (Table 5). In the aMDs, which sample the equivalent to longer time scales, some unbinding events of DCP were observed (Fig. S3). On the other hand, HAOL was released from DhaA31 significantly more frequently than DCP (*P* value 0.013; Tables 5 and 6). The residence times of DCP and HAOL provided corroborative indications of this difference, with HAOL spending more time outside the protein than DCP (Table 5). These simulations thus confirm the remarkable dissimilarity between the release processes of the two products, and are in good agreement with the known fact that the release of DCP from DhaA31 is the slowest step in the catalytic cycle that limits the hydrolytic conversion of TCP by the enzyme [28,36].

Linear interaction energy (LIE) was calculated in all MD simulations to analyze the interactions of the substrates and products with DhaA31. This method evaluates the overall interaction energy of a ligand with the protein in terms of its polar and nonpolar contributions. Here, we have computed these two components and analyzed them separately based on the distance of the ligand to the active site. The results (Fig. S4) show histogram distributions of those distances with several main peaks. These peaks correspond to protein regions more densely populated by the ligands with which strong interactions were formed during the simulations, as described previously [36]. The energy profiles in terms of the ligand location were quite similar for both TCP and CHA substrates and both DCP and HAOL products. The most interesting differences concerned the tunnel and the active site regions (for distances < 13 Å). Here, the CHA and HAOL exhibited stronger van der Waals interactions than their homologs TCP and DCP, respectively. On the other hand, DCP presented significantly stronger electrostatic interactions at the active site than HAOL. These differences clarify some of the observations mentioned above regarding the transport of the ligands through DhaA31's main tunnel. The stronger van der Waals interactions with the tunnel residues presented by CHA, with respect to TCP, explain its faster binding, while the stronger electrostatic interactions shown by DCP, with respect to HAOL, are in good agreement with its slower release.

Overall, the results from our simulations showed that DhaA31 has a different ability for binding the two substrates, as well as for releasing the two alcohol products, and it favors the transport of the CHA/HAOL pair as compared to the TCP/DCP pair. This might lead to the expectation that enlarging the access tunnel would more significantly improve the catalytic rates with TCP than those with CHA. Surprisingly, the opposite was observed. As discussed below, to explain these observations not only the transport processes of the ligands but (mainly) other more complex factors determining all other steps of the catalytic cycle must be taken into account.

Analysis of binding kinetics using a newly prepared TCP-like fluorescent probe

The binding of the CHA-like probe to the DhaA130 variants was correlated with the catalytic turnover number of the corresponding DhaA31 variants with the CHA substrate. Aiming at clarifying whether this might also be achieved with TCP, we have designed a new fluorescent probe to mimic the structure of this substrate (Fig. 2), which was chemically synthesized and characterized (see Supporting Information). This TCP-like probe was utilized for the determination of the binding kinetics with the DhaA130 variants. Initially, we attempted to monitor the TCP-like probe's binding kinetics with the previously well-characterized DhaAWT+H272F and DhaA31 + H272F (DhaA130) proteins. However, the binding experiments with these

Table 5. Rates of main tunnel (p1) opening and ligand transport, and residence time percentages of the substrates, TCP and CHA, and the products, DCP and HAOL, in the simulations with DhaA31.

			Transport rates[b] (events per simulation)		Residence time[c] (%)		
Method	Substrate	Tunnel opening[a] (%)	Binding	Release	Inside	Mouth	Outside
MD	TCP	31.4 ± 8.3	0.5 ± 0.6	0.0 ± 0.0	2.6 ± 1.9	6.7 ± 2.1	90.7 ± 3.1
	CHA	27 ± 12	0.8 ± 1.0	0.3 ± 0.5	8.5 ± 5.2	11.9 ± 1.7	79.6 ± 5.2
aMD	TCP	44.2 ± 5.1	0.8 ± 0.5	0.0 ± 0.0	8.6 ± 2.6	5.2 ± 1.6	86.1 ± 2.9
	CHA	50.0 ± 9.0	1.6 ± 0.9	0.3 ± 0.5	26.3 ± 3.8	8.5 ± 2.4	65.2 ± 5.5

	Product		Release	Rebinding	Inside	Mouth	Outside
MD	DCP	58.5 ± 9.6	0 ± 0	0.0 ± 0.0	100.0 ± 0.0	0.0 ± 0.0	0.0 ± 0.0
	HAOL	56 ± 12	0.5 ± 0.6	0.3 ± 0.5	72.7 ± 20.3	0.7 ± 0.4	26.6 ± 20.0
aMD	DCP	33.5 ± 2.8	0.4 ± 0.6	0.1 ± 0.3	82.1 ± 6.7	2.0 ± 0.82	15.9 ± 6.1
	HAOL	31.5 ± 6.9	1.1 ± 0.6	0.4 ± 0.7	30.3 ± 11.8	2.8 ± 0.64	66.9 ± 11.9

[a]Tunnel opening rates refer to the ratio of snapshots containing the tunnel with radius ≥ 1.4 Å. [b]Transport rates refer to the average number of events per simulation of full binding (the molecule entering from the exterior to within 6 Å of the active site) or full release (leaving the protein interior to distances > 20 Å). [c]Residence times are defined as follows: inside for the distances from the active site ≤ 9 Å, at the tunnel mouth for 9 Å < distances < 13 Å, and outside for the distances ≥ 13 Å. Values were calculated over the 4 × 200 ns MD and 8 × 100 ns aMD simulations with TCP, CHA, and HAOL, and over 8 × 200 ns MD and 16 × 100 ns aMD simulations with DCP. The SD values are presented.

Table 6. Transport rates of TCP and CHA substrates, and DCP and HAOL products in the simulations with DhaA31.

	Transport rates[a] (events per simulation)	
Substrate	Binding	Release
TCP	0.8 ± 0.5	0.0 ± 0.0
CHA	1.6 ± 0.9	0.3 ± 0.5

	Transport rates[a] (events per simulation)	
Product	Release	Rebinding
DCP	0.4 ± 0.6	0.1 ± 0.3
HAOL	1.1 ± 0.6	0.4 ± 0.7

[a]Transport rates refer to the average number of events per simulation of a full binding (the molecule entering from the exterior to within 6 Å of the active site) or a full release (leaving the protein interior to distances > 20 Å). Values were calculated over the 8 × 100 ns aMD simulations with TCP, CHA, and HAOL, and over 16 × 100 ns aMD simulations with DCP. The SD values are presented.

variants were unsuccessful, probably due to extremely slow binding rates (Table 7). Further binding experiments were therefore conducted with the variant DhaAHT (DhaAWT + K175M + C176G + Y273L + H272F), which has a very wide access tunnel, and significantly higher binding rates with previously tested fluorescent ligands [32,37]. The binding of the TCP-like probe to DhaAHT was successfully observed, however, it was nearly five orders of magnitude slower than the binding of the CHA-like probe to this protein. Similarly, we observed a very slow binding of the TCP-like probe to DhaA130 + Y176A, which is the DhaA130 variant with the widest p1 tunnel. To corroborate the slow binding of the TCP-like probe, a new variant with an even wider access tunnel was constructed by introducing a K175M mutation to DhaA130 + Y176A. The binding rate of the TCP-like probe to the resulting variant, DhaA130 + Y176A+K175M, nearly doubled but remained much slower than the CHA-like probe's binding (Table 7).

These results demonstrate that the TCP-like probe does not reliably depict the enzymatic activity of the HLD variants with TCP. While TCP was best catalyzed by variants with narrow tunnels, the binding of that probe was only possible with variants with wider tunnels. This suggests that the binding of both CHA- and TCP-like probes is directly related to the accessibility of the enzyme's active site, which explains why the branched TCP-like probe has much lower binding rates than the CHA-like probe.

Discussion

It has been demonstrated that the molecular tunnels play important roles in the enzymatic catalytic cycle, and therefore the tunnel-lining residues are potential hotspots for engineering the enzymes' properties [6].

The engineering of access tunnels has emerged as an effective approach for fine-tuning the properties of target proteins as well as for *de novo* designing of catalysts. Mutations of tunnel residues can modulate enzyme properties including catalytic activity [28,41], enantioselectivity [42], stability [29], and substrate specificity [30,43]. In this study, Y176 was successfully identified by computational methods as a hotspot residue markedly influencing the properties of DhaA31's access tunnel (geometry, dynamics, and physicochemical nature), and it was subjected to site-saturation mutagenesis.

The mutagenesis of the selected hotspot residue Y176 led to the identification of new enzyme variants with modified binding efficiency toward the CHA-like probe. The structural characterization of the selected variants harboring substitutions at the targeted tunnel position revealed that they did not significantly differ from DhaA31 in folding, but their thermostability varied substantially. The difference in melting temperatures between the most and least thermally stable mutants (DhaA31 + Y176L and DhaA31 + Y176V) was 13.9 °C, which is remarkable for a single-point mutation. We have previously demonstrated that engineering tunnel residues might have a large impact on the protein' stability as well as their tolerance to organic co-solvents [29]. This can be explained by the repacking of the tunnel-lining residues: when the number of contacts within the protein tunnels is increased, the free energy of the folded state is lowered, thus leading to a greater stability. The mutagenesis of the residue Y176 in the inactive variant DhaA130 (DhaA31 containing a mutation of the catalytic base, H272F) has substantially affected the binding kinetics of the fluorescent probe to the selected variants. For instance, the single-point mutation Y176A accelerated the binding of the CHA-like probe (TMR) by three orders of magnitude, with a binding rate constant of 405 $M^{-1}\cdot s^{-1}$, as compared to the template that displayed a binding rate constant of 0.39 $M^{-1}\cdot s^{-1}$. Interestingly, the effects of the mutations on the tunnel geometry of the static structures provided similar trends as the ensemble obtained from the molecular dynamics (MD) simulations, namely the rates of tunnel opening. The binding of the CHA-like probe was highly correlated with the bottleneck radius and the opening rates of the p1 tunnel, which indicates that the tunnel geometry and opening rate are major factors determining the binding of this probe. The binding rates of the TCP-like probe were 3–4 orders of magnitude slower than those of the CHA-like probe to the same variants. This was probably due to the much higher steric hindrance of the branched TCP-like probe that impaired its ability to penetrate the molecular tunnels and reach the active site of the enzymes, as compared to the linear chain of the CHA-like probe.

Table 7. Apparent second order rate constants for the binding of the TCP-like and CHA-like probes to the DhaA variants[a].

	Binding rate constant, k_{bind} ($M^{-1}\cdot s^{-1}$)	
Enzyme	TCP-like probe	CHA-like probe
DhaAWT + H272F	–[b]	56.70 ± 2.30[c]
DhaA130	–[b]	0.39 ± 0.01[c]
DhaAHT	27.8 ± 2.1	(3.80 ± 0.14) × 10^{6}[c]
DhaA130 + Y176A	0.46 ± 0.015	405.0 ± 48.9
DhaA130 + Y176A + K175M	0.84 ± 0.039	1045.8 ± 31.05

[a]All the tested variants contained the H272F mutation. [b]No binding was detected under the experimental conditions. [c]Data from previous work [37]. The SEM values are presented.

Surprisingly, the mutations' effects on the enzyme variants' catalytic efficiencies toward the two chemically rather similar substrates, CHA and TCP, showed opposite trends. The opening of the tunnel by the mutagenesis of Y176 increased the catalytic efficiency toward CHA but reduced the efficiency toward TCP. This clearly demonstrates that the effects of the tunnel engineering are *strictly* ligand-specific. Different ligands possessing specific geometries and physicochemical properties may require a different composition and geometry of the access tunnels. This is partly due to the fact that the tunnel modification has a different impact on the individual steps of the catalysis, which needs to be carefully taken into account. In the case of the HLDs, the catalytic cycle includes diverse steps (Fig. 1), which can turn the enzyme optimization quite a challenging task.

The linear monohalogenated substrate CHA is very similar to the DhaAWT's natural substrate, 1-chlorobutane. The enzyme has evolutionarily been adapted to catalyze this substrate, which is easily degradable due to the single halogen atom bound at the terminal carbon atom of the flexible linear alkyl chain [44,45]. Here, we have shown that the hydrolysis of the alkyl-enzyme intermediate is the rate-limiting step for the conversion of CHA by the template enzyme DhaA31. This means that enlarging the access tunnel is likely to increase the access of water molecules to the active site, which may result in the improvement of the hydrolytic step. This may explain why the activity of the DhaA31 variants toward CHA improved, up to a certain point, with increasing the bottleneck radius of the main tunnel. For variants carrying the substitutions Y176S and Y176A and exhibiting the largest bottleneck radii, the catalytic efficiency decreased again (Table 2 and Fig. 6), which may be due to a change in the rate-limiting step.

Concerning TCP, this branched polyhalogenated substrate is a man-made compound for which no good natural biocatalyst is known. The three chlorine atoms on the adjacent carbons sterically hinder the nucleophilic attack. A previous study has shown that the rate-limiting step for the conversion of this substrate by DhaA31 is the product release [28]. Hence, it could be expected that enlarging the access tunnel would favor the DCP product release and improve catalysis. This was, however, not confirmed. A comprehensive computational work [36] has recently shown that the hydrolysis of TCP was enhanced from DhaAWT to DhaA31 due to the substantial improvement of the S_N2 step, which was initially the limiting step in DhaAWT. That study demonstrated that the mutations V245F and C176Y were responsible for such improvements. These mutations caused a tighter confinement of the TCP substrate in the active site and favored its orientation to increase the probability of the S_N2 reaction, and at the same time decreased the respective energy barrier [36]. In the current study, we observed that the mutation of the bulky Y176 to a smaller amino acid resulted in a lower catalytic efficiency, which suggests that the S_N2 step, that had been improved from DhaAWT, was probably hampered again, either due to the increase in the unproductive conformations of TCP in the active site or due to a higher competition with water molecules. This may also explain why the TCP hydrolysis was impaired further by enlarging the access tunnel. The only mutation that slightly improved the catalysis with TCP was Y176L. This mutation was shown to cause a narrowing of the tunnel bottleneck and a decrease in the opening rates of the free enzyme. However, as we observed before (this study and Ref. [36]), the presence of a ligand can induce tunnel opening, and in fact it is possible that the Y176L mutation may have facilitated the product release, which was the limiting step for DhaA31. This might explain the enhancement of the catalytic process observed with the Y176L mutant.

Our MD simulations have revealed that DhaA31 can better transport the CHA/HAOL pair than the TCP/DCP one. This fact may contribute to its higher catalytic efficiency with CHA as compared to TCP, and to the different kinetic profiles toward these two substrates. Likewise, the interactions of those ligands with the protein may also partially explain their different kinetics. As mentioned above, DhaAWT seems to have evolved to better accommodate and hydrolyze linear haloalkanes than the branched polyhaloalkanes, and DhaA31 bears this heritage. Moreover, the requirements for improving the limiting step in the conversion of CHA are substantially less complex, and it could be improved 10-fold by simply increasing the accessibility of the solvent to the enzyme's active site to a certain extent. This explains why the tunnel engineering was far more straightforward and successful for CHA. Conversely, the catalysis of TCP requires a delicate balance between the S_N2 reaction and the product release [36], but these steps have very different requirements: while the product release is favored by a larger access tunnel, the S_N2 is disfavored by a larger active site and by the competition with water molecules [28,36]. This makes the engineering of a biocatalyst targeting TCP extremely challenging.

To the best of our knowledge, this is the first study showing opposite effects of the mutations of a tunnel residue on the catalytic efficiency toward two different substrates. This result is remarkable considering that the mutated residue is not in direct contact with the substrates in their reactive complexes, but is lining the pathway connecting the active site with the protein surface. Our understanding of the molecular mechanisms of substrate binding and product release is still very limited, and we are at the very beginning of rationally designing optimal tunnels for specific ligands. Along this line, two new CAVER-based [34] software tools – *CaverDock*, for predicting the trajectory and energy profile of a ligand travelling along a tunnel (https://loschmidt.chemi.muni.cz/caverdock/), and *Cavetta*, for performing rational mutations on the tunnel-lining residues (https://loschmidt.chemi.muni.cz/cavetta/) – are being developed in our laboratory for computationally aiding the tunnel engineering. The approach undertaken in this work involved a semi-rational strategy, which included the identification of a hotspot residue by computational methods, the site-saturated mutagenesis of the identified hotspot, and a screening for identifying potentially interesting mutants (Fig. S5A). In a fully rational approach, the available computational tools would be used for *in silico* mutagenesis and to study the mutants' properties to identify the promising ones. Such a workflow (Fig. S5B) would decrease the experimental burden and simultaneously increase the chances of success. In time, we hope that the new computational tools and the accumulated knowledge on the design of enzyme tunnels will facilitate the task of protein engineers to create efficient and stable biocatalysts.

In summary, our results showed that the geometry and dynamics of the access tunnels may have different effects on the binding and catalysis of different ligands. Moreover, our findings demonstrated that the enzyme tunnels must be engineered by taking into account not only the geometry, dynamics, and physicochemical properties of particular residues, but also how the mutations may affect critical steps of the catalytic cycle,

which can be highly dependent on the substrate. Thus, a careful ligand-specific design of these tunnels may be necessary for a successful development of robust and efficient biocatalysts with buried active sites.

Materials and methods

Molecular dynamics with unbound enzymes

System preparation and molecular dynamics

The crystal structure of DhaA31 was obtained from the Protein Data Bank [46] (PDB entry 3RK4) and the structure was prepared as previously described [36]. The system was hydrated with a TIP3P [36] truncated octagonal box of water molecules with edges 10 Å away from the original system. The ff12SB force field [48–51] was used. The PMEMD.CUDA [52,53] module of AMBER 12 [54] was used for running the MD simulations. A cycle of equilibration minimization and dynamics was performed, prior to the production dynamics, and the production MD simulations were run with no restraints for 500 ns, as described previously [36]. Independent minimization-equilibration-production sequences were performed in quadruplicate.

The accelerated MD (aMD) method consists of adding a boost of energy to decrease the depth of the energy basins and thus increase the transitions between conformational states [55,56]. Since the energy barriers are reduced, the conformational sampling is enhanced. This method has been used to explore a greater conformational space of biomolecules than would be possible with the classical MD, being equivalent to timescales more than three orders of magnitude larger. Hence, it can be very useful for studying systems with slow conformational dynamics (μs-ms time scales) [57–63]. Dual torsional and total potential energy boosts were applied to our systems with parameters calculated as previously described [36]. The aMD simulations were carried out with the PMEMD.CUDA [52,53] module of AMBER 12 [54]. They were performed without any constraints after the systems were fully equilibrated, as previously described for the MD simulations, and run in a total of four replicates of 200 ns each. Post-simulation treatment and analysis, namely structure alignment and calculation of RMSD, distances and linear interaction energies, were performed using the CPPTRAJ [64] module of AmberTools 14 [65], and the trajectories were visualized using PYMOL 1.7.4 [66] and VMD 1.9.1 [67].

Tunnel calculation

CAVER version 3.02 [34] was used to calculate the tunnels in the static structures and all simulations of the proteins. The tunnels were calculated for every snapshot of each simulation using a probe radius of 1.0 Å, a shell radius of 3 Å, and shell depth 4 Å. The starting point for the tunnel search was a point in the center of the active site cavity, defined by the geometric center of four atoms from surrounding residues (Y176-C_β, F205-C_α, L209-C_α, and H272-C_α for DhaA31, or equivalent atoms in the mutants). This point is hereafter regarded as the center of the active site. The clustering of the tunnels during the MD and aMD simulations was performed by the average-link hierarchical Murtagh algorithm, with a weighting coefficient of 1 and clustering threshold of 5.0. Approximate clustering was allowed only when the total number of tunnels was higher than 100 000 and it was performed using 15 training clusters. A tunnel was considered open when the radius of its narrowest point, the bottleneck, was ≥ 1.4 Å.

Simulations with mutant enzymes

Mutagenesis with Rosetta and molecular dynamics

The crystal structure of DhaA31, treated as previously described, was renumbered to start from the position 1 and minimized by Rosetta using *minimize_with_cst* module, as previously described [39]. Both backbone and side chain optimizations were enabled (*sc_min_only false*), the distance for full atom pair potential was set to 9 Å (*fa_max_dis* 9.0), standard weights for the individual terms in the energy function were used (force field also called *score12* [39]) with constraint weight 1 (*constraint_weight* 1.0). The minimized DhaA31 structure was then used for the prediction of the single-point mutants: Y176A, Y176C, Y176L, Y176S, and Y176V. To calculate the most stable conformer of each mutant, Protocol 16 was followed using the *ddg_monomer* module of Rosetta as previously described [39], incorporating the backbone flexibility. The soft-repulsive design energy function (*soft_rep_design weights*) was used for repacking side chains and backbone minimization (*sc_min_only false*). The optimization was performed on the whole protein without distance restriction (*local_opt_only false*). The previously generated constraints *cst* file was used during minimization (*min_cst true*) to impose a restraint of 0.5 Å on the C_α atoms. The optimization was performed in three rounds with ever-increasing weight on the repulsive term (*ramp_repulsive* true). The structure with the lowest energy (*mean false*, *min true*) was selected from the 50-iteration cycle (*iterations 50*) and used as the static structure of the respective mutant.

The output PDB files from Rosetta were used to prepare the topology and trajectory input files for performing the MD simulation, as described above. The MD simulations were carried out without any constraints and with the same settings as previously described, but in this case in duplicate runs of 200 ns.

Molecular dynamics with ligands

System preparation and molecular dynamics

The structures of TCP, CHA, DCP, and HAOL were constructed and minimized using Avogadro 1.1.1 [68], optimized by the R.E.D. server [69] with the Hartree–Fock

method and 6-31G* basis set and the multi-orientation RESP fitting performed with the RESP-A1A charge model. The initial structures of DhaA31 with the CHA and TCP substrates were prepared using PYMOL 1.7.4 by manually placing three molecules of the substrate (corresponding to the experimental concentration of ca. 0.01 M) at distances ≥ ca. 5.0 Å away from any atom of the protein, each along with a different Cartesian axis. The systems containing the DCP and HAOL products were prepared by including the chloride ion present at the halide-binding site of the crystal structure of DhaA31, and those alcohol products docked into the active site by AutoDock 4 [70]. The structures of DhaA31 complexed with the ligands were hydrated with a truncated octagonal box of TIP3P water molecules with the edges 12 Å away from the protein atoms in the case of the substrates, and a box of water with the edges 10 Å away from the protein in the case of the products. The complete procedure has been described in detail previously [36].

Unrestrained production MD and aMD simulations were run after an equilibration cycle, for 200 and 100 ns, respectively, using the same setting as described above. Independent MD and aMD simulations were performed with each system depending upon the observation of transport events: four MDs with TCP, CHA and HAOL and eight MDs with DCP, and eight aMDs with TCP, CHA and HAOL and 18 aMDs with DCP.

Construction of site-saturation mutagenesis library and site-directed mutagenesis

Site-saturation mutagenesis was performed at the target position Y176 in an inactive DhaA31 construct, here referred as pET21::*dhaA130,* using QuikChange Multi Site-Directed Mutagenesis Kit (Stratagene, La Jolla, CA, USA) according to manufacturer's protocol. A set of oligonucleotides (Sigma Aldrich, St. Louis, MO, USA): 5′ GTGCTCTGCCGA AANNKGTCGTGCGTCCGCTGAC 3′ (forward) and 5′ CGGACGCACGACMNNTTTCGGCAGAGCACCTTC 3′ (reverse) were used to carry out the mutagenesis. In selected pET21::*dhaA130* variant genes, the phenylalanine at the position 272 was back mutated to histidine which was carried out using QuikChange™ Site-Directed Mutagenesis Kit (Stratagene), to reconstitute the active form of corresponding enzymes. The specific complementary oligonucleotide set was designed to encode the substitution F272H in selected *dhaA130* variant genes 5′ GGTTGATATCGGCCCGGGT CTGCATTTTCTGCAAGAAG 3′ (forward) and 5′ GTTA TCTTCTTGCAGAAAATGCAGACCCGGGCCGATATC 3′ (reverse). The resulting PCR products were then treated by methylation-dependent endonuclease *Dpn*I for 1 h at 37 °C. The generated plasmids were transformed into *Escherichia coli* XJb(DE3) cells (ZymoResearch, Orange, CA, USA) and XL-1 Blue super chemocompetent cells (Stratagene) using the standard electroporation protocol [71]. Candidates from the generated library were randomly selected for DNA sequencing (GATC, Konstanz, Germany). The nucleotide sequences of the variants constructed by site-directed mutagenesis were also confirmed by DNA sequencing.

Cultivation in microtiter plates (MTP) and library screening

Sterile MTP wells were filled with 550 μL of LB medium supplemented with ampicillin at a final concentration of 100 $\mu g \cdot mL^{-1}$, and each well was inoculated with a single transformant using a sterile tooth-pick. Four wells were inoculated with *E. coli* XJb(DE3) cells carrying the *dhaA130* construct to serve as controls in measurements of its binding kinetics, and four with *E. coli* XJb(DE3) cells containing the *dhaA106 + H272F* construct [37] to serve as positive controls during the library screening. Cultures were grown overnight at 37 °C with shaking at 180 rpm. After 14 h cultivation, a replicate plate was created by adding 50 μL of each culture from the cultivation plate to 50 μL of 30% glycerol. To 300 μL of each grown culture in the cultivation plate, we then added 700 μL of fresh LB medium supplemented with ampicillin, L-arabinose at 3 mM and isopropyl β-D-1-thiogalactopyranoside (IPTG) at 0.5 mM concentration. MTPs were cultivated at 30 °C for 5 h, then the cell cultures were harvested and frozen at −80 °C. The constructed library was screened using the FP method previously optimized using cell-free extracts of DhaA enzyme variants prepared in larger volumes [37]. In this study, cell-free extracts of DhaA130 and DhaA106 + H272F were prepared in MTPs and the FP assay was fine-tuned to catch the binding rates of the TMR probe to target proteins directly in the cell-free extract in the MTP. For screening the constructed library, MTPs were defrosted, incubated at room temperature for 15 min, then the cell pellets were rinsed by adding 200 μL of phosphate-buffered saline (pH 7.4) to each well. Cell debris was removed from the lysate by centrifugation at 1600 ***g*** for 20 min after 1 h incubation at room temperature. 140 μL portions of cell lysates were transferred to wells of black polypropylene MTPs (Nunc, Roskilde, Denmark) and 0.1% CHAPS detergent was added to each well. In one of the wells, 140 μL of PBS buffer instead of cell lysate was added with detergent to measure the FP of the free probe. Just before the measurements began, the HaloTag TMR probe (Promega, Madison, WI, USA) was added to each well at a final concentration of 10 nM and the plate was carefully sealed with a sealing tape (MiTeGen, Ithaca, NY, USA) to minimize evaporation of samples during the measurements. The excitation/emission wavelengths were set to 544/580 nm for the TMR probe. The measurements were conducted using an Infinite F500 plate reader (Tecan, Männedorf, Switzerland) for 3 days for each MTP as very slow binding was noted for template DhaA130 in cell-free extracts. Altogether, 140 colonies were screened for modified binding rates in comparison to the template; the

number of tested colonies represented > 98% of library coverage. The screening resulted in the identification of candidates displaying varied binding rates relative to the template, and the corresponding plasmids were isolated and sent for sequencing (GATC).

Protein expression and purification

The recombinant plasmids of pET21::*dhaA31* or *dhaA130* variants were transformed into chemocompetent *E. coli* BL21(DE3) cells. For initiating protein production, cells were grown at 37 °C to OD_{600} 0.5 in 1 L of LB medium supplemented with ampicillin (100 $\mu g \cdot mL^{-1}$). Expression of the recombinant protein was induced by adding IPTG to a final concentration of 0.5 mM in LB medium. The cells were harvested after the overnight expression at 20 °C by centrifugation at 3700 ***g*** at 4 °C for 10 min. During harvesting, the cells were washed with a 20 mM potassium phosphate buffer (pH 7.5) with 10% glycerol, re-suspended in the same buffer and frozen at −80 °C. The defrosted cell suspension was sonicated using a UP200S homogenizer (Hielscher, Teltow, Germany), according to the manufacturer's instructions. The disrupted cells were centrifuged at 21 000 ***g*** at 4 °C for 1 h. The crude extract was collected, filtered, and applied to a Ni-NTA Superflow Cartridge (Qiagen, Hilden, Germany) in equilibrated buffer (20 mM phosphate buffer pH 7.5 containing 0.5 M NaCl and 10 mM imidazole). Unbound and weakly bound proteins were washed out with the buffer containing 10 mM imidazole. The target enzyme was eluted by purification buffer containing 300 mM imidazole. The eluted protein was dialyzed overnight against 50 mM phosphate buffer, pH 7.5. The purity of the resulting recombinant protein was checked by SDS-polyacrylamide gel electrophoresis (SDS/PAGE), followed by staining with Coomassie brilliant blue R-250 dye (Fluka, Buchs, Switzerland). The concentrations of the purified proteins were determined using Bradford reagent and bovine serum albumin as a standard (Sigma-Aldrich, St. Louis, MO, USA).

Circular dichroism (CD) spectroscopy

Circular dichroism spectra of the DhaA31 and DhaA130 variants were collected at room temperature (20 °C) from 185 to 260 nm, at 100 $nm \cdot min^{-1}$, with a 1 s response time and 2 nm bandwidth using a Chirascan spectropolarimeter (Applied Photophysics, Surrey, UK). A 0.1 cm quartz cuvette containing enzyme in a 50 mM potassium phosphate buffer (pH 7.5) was used for measurement. Each spectrum represented the average of five individual scans, corrected for the absorbance caused by the buffer. CD data were expressed in terms of the mean residue ellipticity. Thermal unfolding of DhaA31 and DhaA130 variants was followed by monitoring ellipticity at 222 nm over the temperature range of 20–80 °C, with 0.1 °C resolution, at a heating rate of 1 $°C \cdot min^{-1}$. Recorded denaturation curves were fitted to sigmoidal curves using ORIGIN 8.0 software (OriginLab, Northampton, MA, USA). The midpoint of the thermal transition was regarded as the melting temperature (T_m).

Binding kinetics

Fluorescence polarization measurements were acquired using an Infinite F500 plate reader (Tecan), as described previously [37]. The HaloTag TMR probe was purchased from Promega Corporation, while the TCP-like probe was chemically synthesized in the laboratory, and a 5 mM stock was prepared by dissolving it in DMSO. The binding between the HaloTag TMR/TCP-like probe and the purified DhaA130 variants was monitored by changes in the FP over time at room temperature with $\lambda_{ex}/\lambda_{em}$ set to 544/580 nm. Each DhaA variant was always in excess relative to the fixed concentration of the probe: TMR (10 nM) and DhaA130 (90 μM), DhaA130 + Y176L (72 μM), DhaA130 + Y176C (12 μM), DhaA130 + Y176V (5 μM), DhaA130 + Y176S (4.9 μM), and DhaA130 + Y176A (4 μM); TCP-like probe (10 nM or 50 nM) and DhaAHT (5 μM), DhaA130 + Y176A (50 μM), and DhaA130 + Y176A + K175M (50 μM). The apparent rate constants were calculated using ORIGIN 8.0 software (OriginLab) by fitting the experimental data to a kinetic model of a pseudo-first-order rate reaction, then dividing the determined pseudo-first-order rate constants by the concentration of the reactant in excess to obtain apparent second-order rate constants.

Steady-state kinetics

The steady-state kinetics of DhaA31 variants (Y176C, Y176L, Y176V, Y176S, and Y176A) with TCP and CHA were measured using a VP-ITC isothermal titration microcalorimeter (MicroCal, Piscataway, NJ, USA) at 37 °C. To measure their steady-state kinetics with TCP, the enzymes were dialyzed against a 100 mM glycine buffer (pH 8.6) overnight. The same buffer was used to dissolve the substrate to a final concentration of 9.7–11.3 mM. A reaction mixture vessel of the microcalorimeter was filled with 1.4 mL of enzyme solution at the concentration of 0.017–0.21 $mg \cdot mL^{-1}$. The enzyme was titrated in 150-s intervals in the vessel with ever-increasing amounts of the substrate, while pseudo-first-order conditions were maintained. Every injection increased the substrate concentration, leading to a further increase in the enzyme reaction rate (an increase of heat generated) until the enzymatic reaction was saturated. A total of 28 injections were carried out during the titration. The reaction rates reached after every injection (in units of thermal

power) were converted to enzyme turnover. To measure the steady-state kinetics toward CHA, the substrate was dissolved in 100 mM glycine buffer (pH 8.6) at a final concentration of 0.14–0.53 mM and allowed to reach thermal equilibrium in the reaction cell (1.4 mL). The reaction was initiated by injecting 10 μL of the target enzyme solution. Each reaction was allowed to proceed to completion. The integrated total heat of reactions was divided by the amount of the injected substrate. Substrate concentrations were verified by gas chromatography (Finnigan, San Jose, CA, USA). The plots of the calculated enzyme turnover versus the TCP concentration and the calculated rate of CHA depletion versus its concentration were fitted by nonlinear regression to kinetic models describing Michaelis–Menten dependence (Eqn 1), substrate inhibition (Eqn 2), or cooperativity and substrate inhibition (Eqn 3) using ORIGIN 8.0 software (OriginLab).

$$\frac{v}{V_{\mathrm{lim}}} = \frac{[\mathrm{S}]}{K_{\mathrm{m}} + [\mathrm{S}]}, \tag{1}$$

$$\frac{v}{V_{\mathrm{lim}}} = \frac{[\mathrm{S}]}{K_{\mathrm{m}} + [\mathrm{S}]\left(1 + \frac{[\mathrm{S}]}{K_{\mathrm{si}}}\right)}, \tag{2}$$

$$\frac{v}{V_{\mathrm{lim}}} = \frac{[\mathrm{S}]}{K_{0.5}^{n} + [\mathrm{S}]^{n}\left(1 + \frac{[\mathrm{S}]}{K_{\mathrm{si}}}\right)}. \tag{3}$$

Here, K_{m} is the Michaelis constant, $K_{0.5}$ is the substrate concentration at half maximum velocity, n is the Hill coefficient, K_{si} is the substrate inhibition constant, and k_{cat} is the catalytic constant where $k_{\mathrm{cat}} = V_{\mathrm{lim}}/[\mathrm{E}]$.

Pre-steady-state kinetics

In rapid quench-flow experiments, reactions were started by rapidly mixing 75 μL DhaA31 enzyme with 75 μL substrate solution (both in glycine buffer, pH 8.6) and quenched with 100 μL 0.8 M H_2SO_4 after times ranging from 5 ms to 1.6 s in a QFM 400 instrument (BioLogic, Claix, France). Each quenched mixture was directly injected into 0.5 mL of ice-cold diethyl ether with 1,2-dichloroethane as an internal standard. After extraction, the diethyl ether layer containing non-covalently bound substrate and alcohol product was collected, dried on a short column containing anhydrous Na_2SO_4, and analyzed using an Agilent 7890 gas chromatograph (Agilent, Santa Clara, CA, USA) equipped with a DB-FFAP capillary column (30 m × 0.25 mm × 0.25 μm; Phenomenex, Torrance, CA, USA) and coupled to an Agilent 5975C mass spectrometer (Agilent). The amount of halide in the water phase was measured by ion chromatography using an 861 Advanced Compact chromatograph equipped with a Metrosep A Supp 5 column (Metrohm, Herisau, Switzerland). ORIGIN 6.1 software (OriginLab) was used to fit the kinetic data to burst Eqn (4).

$$\frac{[\mathrm{P}]}{[\mathrm{E}]_0} = A_0(1 - \mathrm{e}^{-k_{\mathrm{burst}}t}) + k_{\mathrm{ss}}t. \tag{4}$$

Chemical synthesis

The TCP-like probe was synthesized using reagent grade reagents and solvents without further purification. Anhydrous solvents (dimethylformamide, dichloromethane, and ethanol) were used and stored over 4 Å molecular sieves as received from commercial suppliers. All reactions were carried out in oven-dried glassware and under a nitrogen atmosphere unless stated otherwise. The flash column chromatography was carried on silica gel (230–400 mesh). TLC plates were visualized under UV and/or with $KMnO_4$. Nuclear magnetic resonance (NMR) spectra were recorded on a Bruker Avance 500 MHz spectrometer (with operating frequencies, 500.13 MHz for ^{1}H, 125.77 MHz for ^{13}C, 470.53 MHz for ^{19}F). The ^{1}H and ^{13}C NMR chemical shifts (δ in p.p.m.) were referenced to the residual signals of the solvent: $CDCl_3$ [7.26 (^{1}H) and 77.16 (^{13}C)]. High-resolution mass spectra were acquired using an Agilent 6224 TOF LC-MS operated in dual electrospray/chemical ionization mode with mass accuracy greater than 2 p.p.m. and applied mass range from 25 to 20 000 Da. Infrared spectra (4000–400 cm^{-1}) were collected using a Bruker Alpha FTIR spectrometer. The solid samples were measured neat and the oily samples as films. Details of the methodology applied in the chemical synthesis of the TCP-like probe are presented in the Dataset S1.

Acknowledgements

The authors express many thanks to Hana Moskalikova (Masaryk University, Brno, Czech Republic) for her help with the collection of rapid quench-flow data. The work was supported by the Grant Agency of the Czech Republic (16-24223S and 17-24321S), the Ministry of Education, Youth, and Sports of the Czech Republic (LO1214, LQ1605, LM2015047, LM2015051, LM2015055, LM2015063), and Masaryk University (MUNI/M/1888/2014). The computational resources were provided by CESNET (LM2015042) and the CERIT Scientific Cloud (LM2015085). SK was supported by the 'Employment of Best Young Scientists for International Cooperation Empowerment' project (CZ.1.07/2.3.00/30.0037), co-financed by the European Social Fund and the State Budget of the Czech Republic. SMM was supported by the SoMoPro II Programme (project BIOGATE, No. 4SGA8519), which is co-financed by the People Programme (Marie Curie action) of the EU's Seventh Framework Programme

according to the REA Grant Agreement No. 291782, and the South Moravian Region. This research was also supported by the RECETOX Research Infrastructure (LM2015051 and CZ.02.1.01/0.0/0.0/16_013/0001761). This publication only reflects the authors' views and the Union is not liable for any use that may be made of the information contained herein.

Conflict of interest

The authors declare that they have no conflicts of interest with the contents of this article.

Author contributions

RC, JB, and JD conceived and designed the study. SMM and JB performed the molecular modeling and analyzed the data. SK, LL, and RC performed the mutagenesis, library screening, protein expression, purification and characterization, steady-state kinetics, and analyzed the data. ZP performed the pre-steady-state kinetics experiments and analyzed the data. PK and KP performed the chemical synthesis. SK and SMM wrote the manuscript. All authors reviewed the results and contributed to finalization of the manuscript.

References

1 Raushel FM, Thoden JB & Holden HM (2003) Enzymes with molecular tunnels. *Acc Chem Res* **36**, 539–548.
2 Huang X, Holden HM & Raushel FM (2001) Channeling of substrates and intermediates in enzyme-catalyzed reactions. *Annu Rev Biochem* **70**, 149–180.
3 Damborsky J, Chaloupková R, Pavlová M, Chovancova E & Brezovsky J (2010) Structure–function relationships and engineering of haloalkane dehalogenases. Handbook of Hydrocarbon and Lipid Microbiology, pp. 1081–1098. Springer, Berlin, Germany.
4 Damborsky J & Brezovsky J (2009) Computational tools for designing and engineering biocatalysts. *Curr Opin Chem Biol* **13**, 26–34.
5 Kingsley LJ & Lill MA (2015) Substrate tunnels in enzymes: structure–function relationships and computational methodology. *Proteins* **83**, 599–611.
6 Prokop Z, Gora A, Brezovsky J, Chaloupkova R, Stepankova V & Damborsky J (2012) Engineering of protein tunnels: the keyhole–lock–key model for catalysis by enzymes with buried active sites. Protein Engineering Handbook, pp. 421–464. Wiley-VCH, Weinheim.
7 Hyde C, Ahmed S, Padlan E, Miles EW & Davies D (1988) Three-dimensional structure of the tryptophan synthase alpha 2 beta 2 multienzyme complex from *Salmonella typhimurium*. *J Biol Chem* **263**, 17857–17871.
8 Pleiss J, Fischer M & Schmid RD (1998) Anatomy of lipase binding sites: the scissile fatty acid binding site. *Chem Phys Lipids* **93**, 67–80.
9 Wade RC, Winn PJ & Schlichting I (2004) A survey of active site access channels in cytochromes P450. *J Inorg Biochem* **98**, 1175–1182.
10 Koudelakova T, Chovancova E, Brezovsky J, Monincova M, Fortova A, Jarkovsky J & Damborsky J (2011) Substrate specificity of haloalkane dehalogenases. *Biochem J* **435**, 345–354.
11 Binda C, Coda A, Angelini R, Federico R, Ascenzi P & Mattevi A (1999) A 30 Å long U-shaped catalytic tunnel in the crystal structure of polyamine oxidase. *Structure* **7**, 265–276.
12 Gora A, Brezovsky J & Damborsky J (2013) Gates of enzymes. *Chem Rev* **113**, 5871–5923.
13 Zhou HX & McCammon JA (2010) The gates of ion channels and enzymes. *Trends Biochem Sci* **35**, 179–185.
14 Marques SM, Brezovsky J & Damborsky J (2016) Role of tunnels and gates in enzymatic catalysis. In *Understanding Enzymes Function, Design, Engineering, and Analysis* (Svendsen A, ed.), pp. 421–463. Pan Stanford Publishing, Singapore.
15 Engel PC (1981) Enzymatic reaction mechanisms: by C Walsh. pp 978. WH Freeman & Co, Oxford. 1979. *Biochem Educ* **9**, 119.
16 Shang BZ, Chang R & Chu JW (2013) Systems-level modeling with molecular resolution elucidates the rate-limiting mechanisms of cellulose decomposition by cellobiohydrolases. *J Biol Chem* **288**, 29081–29089.
17 Bosma T, Pikkemaat MG, Kingma J, Dijk J & Janssen DB (2003) Steady-state and pre-steady-state kinetic analysis of halopropane conversion by a *Rhodococcus* haloalkane dehalogenase. *Biochemistry* **42**, 8047–8053.
18 Jonnalagadda V, Toth K & Richard JP (2012) Isopentenyl diphosphate isomerase catalyzed reactions in D_2O: product release limits the rate of this sluggish enzyme-catalyzed reaction. *J Am Chem Soc* **134**, 6568–6570.
19 De Regil R & Sandoval G (2013) Biocatalysis for biobased chemicals. *Biomolecules* **3**, 812–847.
20 Turner NJ (2009) Directed evolution drives the next generation of biocatalysts. *Nat Chem Biol* **5**, 567–573.
21 Davids T, Schmidt M, Böttcher D & Bornscheuer UT (2013) Strategies for the discovery and engineering of enzymes for biocatalysis. *Curr Opin Chem Biol* **17**, 215–220.
22 Kries H, Blomberg R & Hilvert D (2013) De novo enzymes by computational design. *Curr Opin Chem Biol* **17**, 221–228.
23 Privett HK, Kiss G, Lee TM, Blomberg R, Chica RA, Thomas LM, Hilvert D, Houk KN & Mayo SL (2012)

Iterative approach to computational enzyme design. *Proc Natl Acad Sci USA* **109**, 3790–3795.
24 Siegel JB, Zanghellini A, Lovick HM, Kiss G, Lambert AR, Clair JLS, Gallaher JL, Hilvert D, Gelb MH & Stoddard BL (2010) Computational design of an enzyme catalyst for a stereoselective bimolecular Diels-Alder reaction. *Science* **329**, 309–313.
25 Blomberg R, Kries H, Pinkas DM, Mittl PR, Grütter MG, Privett HK, Mayo SL & Hilvert D (2013) Precision is essential for efficient catalysis in an evolved Kemp eliminase. *Nature* **503**, 418–421.
26 Brezovsky J, Babkova P, Degtjarik O, Fortova A, Gora A, Iermak I, Rezacova P, Dvorak P, Smatanova IK & Prokop Z (2016) Engineering a *de novo* transport tunnel. *ACS Catal* **6**, 7597–7610.
27 Koudelakova T, Bidmanova S, Dvorak P, Pavelka A, Chaloupkova R, Prokop Z & Damborsky J (2013) Haloalkane dehalogenases: biotechnological applications. *Biotechnol J* **8**, 32–45.
28 Pavlova M, Klvana M, Prokop Z, Chaloupkova R, Banas P, Otyepka M, Wade RC, Tsuda M, Nagata Y & Damborsky J (2009) Redesigning dehalogenase access tunnels as a strategy for degrading an anthropogenic substrate. *Nature Chem Biol* **5**, 727–733.
29 Koudelakova T, Chaloupkova R, Brezovsky J, Prokop Z, Sebestova E, Hesseler M, Khabiri M, Plevaka M, Kulik D & Kuta Smatanova I (2013) Engineering enzyme stability and resistance to an organic cosolvent by modification of residues in the access tunnel. *Angew Chem Int Ed* **52**, 1959–1963.
30 Chaloupková R, Sýkorová J, Prokop Z, Jesenská A, Monincová M, Pavlová M, Tsuda M, Nagata Y & Damborský J (2003) Modification of activity and specificity of haloalkane dehalogenase from *Sphingomonas paucimobilis* UT26 by engineering of its entrance tunnel. *J Biol Chem* **278**, 52622–52628.
31 Liskova V, Bednar D, Prudnikova T, Rezacova P, Koudelakova T, Sebestova E, Smatanova IK, Brezovsky J, Chaloupkova R & Damborsky J (2015) Balancing the stability–activity trade-off by fine-tuning dehalogenase access tunnels. *ChemCatChem* **7**, 648–659.
32 Los GV, Encell LP, McDougall MG, Hartzell DD, Karassina N, Zimprich C, Wood MG, Learish R, Ohana RF & Urh M (2008) HaloTag: a novel protein labeling technology for cell imaging and protein analysis. *ACS Chem Biol* **3**, 373–382.
33 Kutý M, Damborský J, Prokop M & Koca J (1998) A molecular modeling study of the catalytic mechanism of haloalkane dehalogenase. 2. Quantum chemical study of complete reaction mechanism. *J Chem Inf Comp Sci* **38**, 736–741.
34 Chovancová E, Pavelka A, Benes P, Strnad O, Brezovsky J, Kozlikova B, Gora A, Sustr V, Klvana M, Medek P *et al.* (2012) CAVER 3.0: a tool for the analysis of transport pathways in dynamic protein structures. *PLoS Comput Biol* **8**, e1002708.
35 Klvana M, Pavlova M, Koudelakova T, Chaloupkova R, Dvorak P, Prokop Z, Stsiapanava A, Kuty M, Kuta-Smatanova I, Dohnalek J *et al.* (2009) Pathways and mechanisms for product release in the engineered haloalkane dehalogenases explored using classical and random acceleration molecular dynamics simulations. *J Mol Biol* **392**, 1339–1356.
36 Marques SM, Dunajova Z, Prokop Z, Chaloupkova R, Brezovsky J & Damborsky J (2017) Catalytic cycle of haloalkane dehalogenases toward unnatural substrates explored by computational modeling. *J Chem Inf Model* **57**, 1970–1989.
37 Kaushik S, Prokop Z, Damborsky J & Chaloupkova R (2017) Kinetics of binding of fluorescent ligands to enzymes with engineered access tunnels. *FEBS J* **284**, 134–148.
38 Verschueren KH, Seljée F, Rozeboom HJ, Kalk KH & Dijkstra BW (1993) Crystallographic analysis of the catalytic mechanism of haloalkane dehalogenase. *Nature* **363**, 693–698.
39 Kellogg EH, Leaver-Fay A & Baker D (2011) Role of conformational sampling in computing mutation-induced changes in protein structure and stability. *Proteins* **79**, 830–838.
40 Stank A, Kokh DB, Fuller JC & Wade RC (2016) Protein binding pocket dynamics. *Acc Chem Res* **49**, 809–815.
41 Ba L, Li P, Zhang H, Duan Y & Lin Z (2013) Semi-rational engineering of cytochrome P450sca-2 in a hybrid system for enhanced catalytic activity: Insights into the important role of electron transfer. *Biotechnol Bioeng* **110**, 2815–2825.
42 Lafaquière V, Barbe S, Puech-Guenot S, Guieysse D, Cortés J, Monsan P, Siméon T, André I & Remaud-Siméon M (2009) Control of lipase enantioselectivity by engineering the substrate binding site and access channel. *ChemBioChem* **10**, 2760–2771.
43 Bühler H, Effenberger F, Förster S, Roos J & Wajant H (2003) Substrate specificity of mutants of the hydroxynitrile lyase from *Manihot esculenta*. *ChemBioChem* **4**, 211–216.
44 Kulakova AN, Stafford TM, Larkin MJ & Kulakov LA (1995) Plasmid pRTL1 controlling 1-chloroalkane degradation by *Rhodococcus rhodochrous* NCIMB13064. *Plasmid* **33**, 208–217.
45 Kulakova AN, Larkin MJ & Kulakov LA (1997) The Plasmid-located haloalkane dehalogenase gene from *Rhodococcus rhodochrous* NCIMB 13064. *Microbiology* **143**, 109–115.
46 Rose PW, Bi C, Bluhm WF, Christie CH, Dimitropoulos D, Dutta S, Green RK, Goodsell DS, Prlić A & Quesada M (2013) The RCSB Protein Data

Bank: new resources for research and education. *Nucleic Acids Res* **41**, D475–D482.
47 Jorgensen WL, Chandrasekhar J, Madura JD, Impey RW & Klein ML (1983) Comparison of simple potential functions for simulating liquid water. *J Phys Chem* **79**, 926–935.
48 Hornak V, Abel R, Okur A, Strockbine B, Roitberg A & Simmerling C (2006) Comparison of multiple Amber force fields and development of improved protein backbone parameters. *Proteins* **65**, 712–725.
49 Joung IS & Cheatham TE III (2008) Determination of alkali and halide monovalent ion parameters for use in explicitly solvated biomolecular simulations. *J Phys Chem B* **112**, 9020–9041.
50 Joung IS & Cheatham TE III (2009) Molecular dynamics simulations of the dynamic and energetic properties of alkali and halide ions using water-model-specific ion parameters. *J Phys Chem B* **113**, 13279–13290.
51 Nguyen H, Maier J, Huang H, Perrone V & Simmerling C (2014) Folding simulations for proteins with diverse topologies are accessible in days with a physics-based force field and implicit solvent. *J Am Chem Soc* **136**, 13959–13962.
52 Götz AW, Williamson MJ, Xu D, Poole D, Le Grand S & Walker RC (2012) Routine microsecond molecular dynamics simulations with AMBER on GPUs. 1. Generalized born. *J Chem Theory Comput* **8**, 1542–1555.
53 Le Grand S, Götz AW & Walker RC (2013) SPFP: speed without compromise—a mixed precision model for GPU accelerated molecular dynamics simulations. *Comput Phys Commun* **184**, 374–380.
54 Case DA, Darden TA, Cheatham ITE, Simmerling CL, Wang J, Duke RE, Luo R, Walker RC, Zhang W, Merz KM *et al.* (2012) AMBER 12. University of California, San Francisco, CA.
55 Hamelberg D, de Oliveira CAF & McCammon JA (2007) Sampling of slow diffusive conformational transitions with accelerated molecular dynamics. *J Chem Phys* **127**, 155102.
56 Hamelberg D, Mongan J & McCammon JA (2004) Accelerated molecular dynamics: a promising and efficient simulation method for biomolecules. *J Chem Phys* **120**, 11919–11929.
57 Pierce LCT, Salomon-Ferrer R, Augusto F de Oliveira C, McCammon JA & Walker RC (2012) Routine access to millisecond time scale events with accelerated molecular dynamics. *J Chem Theory Comput* **8**, 2997–3002.
58 Markwick PR & McCammon JA (2011) Studying functional dynamics in bio-molecules using accelerated molecular dynamics. *Phys Chem Chem Phys* **13**, 20053–20065.
59 Bucher D, Grant BJ, Markwick PR & McCammon JA (2011) Accessing a hidden conformation of the maltose binding protein using accelerated molecular dynamics. *PLoS Comput Biol* **7**, e1002034.
60 de Oliveira CAF, Grant BJ, Zhou M & McCammon JA (2011) Large-scale conformational changes of *Trypanosoma cruzi* proline racemase predicted by accelerated molecular dynamics simulation. *PLoS Comput Biol* **7**, e1002178.
61 Miao Y, Nichols SE, Gasper PM, Metzger VT & McCammon JA (2013) Activation and dynamic network of the M2 muscarinic receptor. *Proc Natl Acad Sci USA* **110**, 10982–10987.
62 Wereszczynski J & McCammon JA (2012) Nucleotide-dependent mechanism of Get3 as elucidated from free energy calculations. *Proc Natl Acad Sci USA* **109**, 7759–7764.
63 Wiesler SC, Weinzierl RO & Buck M (2013) An aromatic residue switch in enhancer-dependent bacterial RNA polymerase controls transcription intermediate complex activity. *Nucleic Acids Res* **41**, 5874–5886.
64 Roe DR & Cheatham TE III (2013) PTRAJ and CPPTRAJ: software for processing and analysis of molecular dynamics trajectory data. *J Chem Theory Comput* **9**, 3084–3095.
65 Case D, Babin V, Berryman J, Betz R, Cai Q, Cerutti D, Cheatham T III, Darden T, Duke R & Gohlke H (2006) AMBER 14. University of California, San Francisco, CA.
66 Schrödinger L. The PyMOL Molecular Graphics System, Version 1.7. 4. Schrödinger, LLC, New York.
67 Humphrey W, Dalke A & Schulten K (1996) VMD: visual molecular dynamics. *J Mol Graph* **14**, 33–38.
68 Hanwell MD, Curtis DE, Lonie DC, Vandermeersch T, Zurek E & Hutchison GR (2012) Avogadro: an advanced semantic chemical editor, visualization, and analysis platform. *J Cheminform* **4**, 17.
69 Vanquelef E, Simon S, Marquant G, Garcia E, Klimerak G, Delepine JC, Cieplak P & Dupradeau F-Y (2011) RED Server: a web service for deriving RESP and ESP charges and building force field libraries for new molecules and molecular fragments. *Nucleic Acids Res* **39**, W511–W517.
70 Morris GM, Huey R, Lindstrom W, Sanner MF, Belew RK, Goodsell DS & Olson AJ (2009) AutoDock4 and AutoDockTools4: automated docking with selective receptor flexibility. *J Comput Chem* **30**, 2785–2791.
71 Sambrook J & Russell D (2001) Molecular Cloning, A Laboratory Manual, 3rd edn. Cold Spring Horbor Laboratory Press, Cold Spring Harbor, NY.

Supporting information

Additional Supporting Information may be found online in the supporting information tab for this article:

Fig. S1. Far-UV CD spectra of the purified DhaA130 and DhaA31 variants.
Fig. S2. Representative structures of DhaA31 with TCP substrates at the initial state and after binding the main tunnel.
Fig. S3. Representative structures of DhaA31 with DCP and Cl^- products at the initial state and after release.
Fig. S4. Linear interaction energy of the substrates, TCP and CHA, and the products, DCP and HAOL, with the protein during the MD simulations with DhaA31.
Fig. S5. Different strategies for computer-assisted design of ligand-specific tunnels.
Dataset S1. Chemical synthesis and characterization of the TCP-like probe
Table S1. Main parameters obtained for the top-ranked tunnels calculated in the MD and aMD simulations of DhaA31.
Table S2. Parameters obtained for p1 tunnel in the simulations of DhaA31.
Table S3. Pearson correlation coefficients between the kinetic parameters and the physicochemical properties of the respective amino acid residue at position 176.